Supplemental Material for: Twist-bend coupling and the torsional response of double-stranded DNA

Stefanos K. Nomidis,[1] Franziska Kriegel,[2] Willem Vanderlinden,[3,2] Jan Lipfert,[2] and Enrico Carlon[1]

[1] *KU Leuven, Institute for Theoretical Physics, Celestijnenlaan 200D, 3001 Leuven, Belgium*
[2] *Department of Physics, Nanosystems Initiative Munich, and Center for NanoScience, LMU Munich, 80799 Munich, Germany*
[3] *KU Leuven, Division of Molecular Imaging and Photonics, Celestijnenlaan 200F, 3001 Leuven, Belgium*

(Dated: May 2, 2017)

CONTENTS

CALCULATIONS OF κ_b AND κ_t IN THE MS MODEL

In this section we present the details of the calculations of κ_b and κ_t, reported in Eqs.(3) amd (4) of the main text. Defining $A_1 = A + \varepsilon$ and $A_2 = A - \varepsilon$, we write the energy of the model as follows

$$\frac{E_{\text{MS}}}{k_B T} = \frac{1}{2}\int_0^L ds \left(A_1\Omega_1^2 + A_2\Omega_2^2 + C\Omega_3^2 + 2G\Omega_2\Omega_3\right) = \frac{E_{\text{TWLC}}}{k_B T} + \int_0^L ds \left[\frac{\varepsilon}{2}\left(\Omega_1^2 - \Omega_2^2\right) + G\Omega_2\Omega_3\right], \tag{S1}$$

where E_{TWLC} indicates the energy of the standard TWLC model and the two additional terms are the contributions from the bending anisotropy ($\varepsilon \neq 0$) and the twist-bend coupling ($G \neq 0$).

As shown in Fig. 1 of the main manuscript, we introduce an orthonormal set of vectors $\{\widehat{\mathbf{e}}_1, \widehat{\mathbf{e}}_2, \widehat{\mathbf{e}}_3\}$ which is associated with every point along the molecule. Here $\widehat{\mathbf{e}}_3$ is the tangent to the curve and $\widehat{\mathbf{e}}_1$ points from the center of the helix towards its minor groove. The third vector is obtained from the relation $\widehat{\mathbf{e}}_2 = \widehat{\mathbf{e}}_3 \times \widehat{\mathbf{e}}_1$. In a relaxed dsDNA molecule the helical axis is completely straight, corresponding to $\widehat{\mathbf{e}}_3(s)$ being constant along the molecule, where $0 \leq s \leq L$ is the arc length. The double helix makes a full turn every $l = 2\pi/\omega_0 \approx 3.4$ nm, which means that $\widehat{\mathbf{e}}_1(s)$ and $\widehat{\mathbf{e}}_2$(s) are rotated by an angle of $\omega_0 s$ with respect to $\widehat{\mathbf{e}}_1(0)$ and $\widehat{\mathbf{e}}_2(0)$. Any deformation from this ideal state can be described by the following differential equation [1]

$$\frac{d\widehat{\mathbf{e}}_i}{ds} = (\omega_0\widehat{\mathbf{e}}_3 + \boldsymbol{\Omega}) \times \widehat{\mathbf{e}}_i, \tag{S2}$$

where $|\omega_0\widehat{\mathbf{e}}_3 + \boldsymbol{\Omega}|\, ds$ is the infinitesimal angle around the direction of the vector $\omega_0\widehat{\mathbf{e}}_3 + \boldsymbol{\Omega}$, by which the set $\{\widehat{\mathbf{e}}_1, \widehat{\mathbf{e}}_2, \widehat{\mathbf{e}}_3\}$ is rotated when going from s to $s + ds$. In general $\boldsymbol{\Omega}(s)$ depends on the position s and it is customary to introduce the three local components as follows $\boldsymbol{\Omega} = \Omega_1\widehat{\mathbf{e}}_1 + \Omega_2\widehat{\mathbf{e}}_2 + \Omega_3\widehat{\mathbf{e}}_3$.

We now need to express $\{\Omega_i\}$ as functions of the vectors $\{\widehat{\mathbf{e}}_i\}$ and their derivatives. For this purpose we use the relations

$$\frac{d\widehat{\mathbf{e}}_1}{ds} = (\omega_0 + \Omega_3)\,\widehat{\mathbf{e}}_2 - \Omega_2\widehat{\mathbf{e}}_3, \tag{S3}$$

$$\frac{d\widehat{\mathbf{e}}_2}{ds} = \Omega_1\widehat{\mathbf{e}}_3 - (\omega_0 + \Omega_3)\,\widehat{\mathbf{e}}_1, \tag{S4}$$

$$\frac{d\widehat{\mathbf{e}}_3}{ds} = \Omega_2\widehat{\mathbf{e}}_1 - \Omega_1\widehat{\mathbf{e}}_2, \tag{S5}$$

which are obtained from Eq. (S2). Next we discretize the model introducing a discretization length a and using the following approximations

$$\frac{d\widehat{\mathbf{e}}_i(s)}{ds} \approx \frac{\widehat{\mathbf{e}}_i(s+a) - \widehat{\mathbf{e}}_i(s)}{a}, \tag{S6}$$

$$\widehat{\mathbf{e}}_i(s) \approx \frac{\widehat{\mathbf{e}}_i(s+a) + \widehat{\mathbf{e}}_i(s)}{2}. \tag{S7}$$

In order to parametrize the rotation of the frame $\{\widehat{\mathbf{e}}_1(s), \widehat{\mathbf{e}}_2(s), \widehat{\mathbf{e}}_3(s)\}$ into $\{\widehat{\mathbf{e}}_1(s+a), \widehat{\mathbf{e}}_2(s+a), \widehat{\mathbf{e}}_3(s+a)\}$, we introduce three Euler angles $\alpha(s)$, $\beta(s)$ and $\gamma(s)$. These angles correspond to a sequence of three elementary rotations: one about $\widehat{\mathbf{e}}_3$, followed by one about $\widehat{\mathbf{e}}_1$ and finally a rotation about $\widehat{\mathbf{e}}_3$, respectively

$$\widehat{\mathbf{e}}_i(s+a) = \sum_{j=1}^{3} R_{ij}(\alpha,\beta,\gamma)\widehat{\mathbf{e}}_j(s), \tag{S8}$$

where R is the product of three rotation matrices

$$R = E_3(\gamma)E_1(\beta)E_3(\alpha) \tag{S9}$$

with

$$E_1(\phi) = \begin{pmatrix} 1 & 0 & 0 \\ 0 & \cos\phi & \sin\phi \\ 0 & -\sin\phi & \cos\phi \end{pmatrix} \qquad \text{and} \qquad E_3(\phi) = \begin{pmatrix} \cos\phi & \sin\phi & 0 \\ -\sin\phi & \cos\phi & 0 \\ 0 & 0 & 1 \end{pmatrix}. \tag{S10}$$

Plugging this into Eq. (S9) gives

$$R = \begin{pmatrix} \cos\alpha\cos\gamma - \sin\alpha\cos\beta\sin\gamma & \sin\alpha\cos\gamma + \cos\alpha\cos\beta\sin\gamma & \sin\beta\sin\gamma \\ -\cos\alpha\sin\gamma - \sin\alpha\cos\beta\cos\gamma & -\sin\alpha\sin\gamma + \cos\alpha\cos\beta\cos\gamma & \sin\beta\cos\gamma \\ \sin\alpha\sin\beta & -\cos\alpha\sin\beta & \cos\beta \end{pmatrix}. \tag{S11}$$

We can now combine the above equations in order to obtain

$$\begin{aligned} \Omega_1^2 &= \widehat{\mathbf{e}}_1 \cdot \frac{d\widehat{\mathbf{e}}_2}{ds} \times \frac{d\widehat{\mathbf{e}}_3}{ds} = \frac{\widehat{\mathbf{e}}_1(s+a) + \widehat{\mathbf{e}}_1(s)}{2} \cdot \frac{\widehat{\mathbf{e}}_2(s+a) - \widehat{\mathbf{e}}_2(s)}{a} \times \frac{\widehat{\mathbf{e}}_3(s+a) - \widehat{\mathbf{e}}_3(s)}{a} \\ &= \frac{1 + \widehat{\mathbf{e}}_1(s+a)\cdot\widehat{\mathbf{e}}_1(s) - \widehat{\mathbf{e}}_2(s+a)\cdot\widehat{\mathbf{e}}_2(s) - \widehat{\mathbf{e}}_3(s+a)\cdot\widehat{\mathbf{e}}_3(s)}{a^2} = \frac{1 + R_{11} - R_{22} - R_{33}}{a^2} \\ &= \frac{(1-\cos\beta)\,[1+\cos(\alpha-\gamma)]}{a^2}, \end{aligned} \tag{S12}$$

$$\Omega_2^2 = \widehat{\mathbf{e}}_2 \cdot \frac{d\widehat{\mathbf{e}}_3}{ds} \times \frac{d\widehat{\mathbf{e}}_1}{ds} = \frac{(1-\cos\beta)\,[1-\cos(\alpha-\gamma)]}{a^2} \tag{S13}$$

and hence

$$\Omega_1^2 + \Omega_2^2 = \frac{2}{a^2}\left(1 - \cos\beta\right), \tag{S14}$$

$$\Omega_1^2 - \Omega_2^2 = \frac{2}{a^2}\left(1 - \cos\beta\right)\cos\left(\alpha - \gamma\right). \tag{S15}$$

The other two terms appearing in Eq. (S1) are

$$\Omega_3^2 = \widehat{\mathbf{e}}_3 \cdot \left(\frac{d\widehat{\mathbf{e}}_1}{ds} - \omega_0 \widehat{\mathbf{e}}_2\right) \times \left(\frac{d\widehat{\mathbf{e}}_2}{ds} + \omega_0 \widehat{\mathbf{e}}_1\right) = \frac{\left(1 + \cos\beta\right)\left[1 - \cos\left(\alpha + \gamma\right) - a\omega_0 \sin\left(\alpha + \gamma\right)\right] + a^2\omega_0^2}{a^2}, \tag{S16}$$

$$\Omega_2\Omega_3 = -\frac{d\widehat{\mathbf{e}}_3}{ds} \cdot \left(\frac{d\widehat{\mathbf{e}}_2}{ds} + \omega_0 \widehat{\mathbf{e}}_1\right) = \frac{\sin\beta\left[2(\cos\gamma - \cos\alpha) + a\omega_0\left(\sin\alpha - \sin\gamma\right)\right]}{2a^2}. \tag{S17}$$

In the continuum limit $a \to 0$, the Euler angles become infinitesimally small, i.e. $\alpha, \beta, \gamma \to 0$. This allows us to approximate

$$1 + \cos\beta \approx 2, \tag{S18}$$

$$\cos\alpha + \frac{a\omega_0}{2}\sin\alpha \approx \cos\left(\alpha - \phi_0\right), \tag{S19}$$

$$\cos\gamma + \frac{a\omega_0}{2}\sin\gamma \approx \cos\left(\gamma - \phi_0\right), \tag{S20}$$

$$\cos\left(\alpha + \gamma\right) + a\omega_0 \sin\left(\alpha + \gamma\right) \approx \cos\left(\alpha + \gamma - 2\phi_0\right), \tag{S21}$$

where we have defined

$$\phi_0 \equiv \frac{a\omega_0}{2} \approx \sin\left(\frac{a\omega_0}{2}\right) \tag{S22}$$

and made use of $\cos\phi_0 \approx 1$. With the above approximations we get

$$\Omega_3^2 = \frac{2}{a^2}\left[1 - \cos\left(\alpha + \gamma - 2\phi_0\right)\right] + \omega_0^2, \tag{S23}$$

$$\Omega_2\Omega_3 = -\frac{1}{a^2}\sin\beta\left[\cos\left(\alpha - \phi_0\right) - \cos\left(\gamma - \phi_0\right)\right]. \tag{S24}$$

Substituting Eqs. (S14), (S15), (S23) and (S24) into (S1) and transforming the integral into a sum over segments of length a ($\int_0^L ds \ldots \approx a\sum_i \ldots$) yields

$$\begin{aligned}\frac{E_{\mathrm{MS}}}{k_B T} = -\frac{1}{a}\sum_i \{&A\cos\beta_i + C\cos\left(\alpha_i + \gamma_i - 2\phi_0\right) - \varepsilon\left(1 - \cos\beta_i\right)\cos\left(\alpha_i - \gamma_i\right) \\ &+ G\sin\beta_i\left[\cos\left(\alpha_i - \phi_0\right) - \cos\left(\gamma_i - \phi_0\right)\right]\}, \end{aligned} \tag{S25}$$

where we have omitted any constant terms. One can simplify this expression by introducing the angles $\psi_i \equiv \alpha_i + \gamma_i - 2\phi_0$ and $\chi_i \equiv \alpha_i - \gamma_i$, so as to obtain

$$\frac{E_{\mathrm{MS}}}{k_B T} = -\frac{1}{a}\sum_i \left[A\cos\beta_i + C\cos\psi_i - \varepsilon(1 - \cos\beta_i)\cos\chi_i - 2G\sin\frac{\chi_i}{2}\sin\frac{\psi_i}{2}\sin\beta_i\right], \tag{S26}$$

where β_i and ψ_i are bending and twist angles, respectively.

The total partition function can be written as

$$Z = \prod_i \left(\int d\beta_i \sin\beta_i d\psi_i d\chi_i\right) e^{-E_{\mathrm{MS}}/k_B T}, \tag{S27}$$

where $\beta_i \in [0, \pi]$ and $\psi_i, \chi_i \in [-\pi, \pi]$. As the total energy is the sum of independent contributions, it is sufficient to

consider the partition function of a single segment

$$Z_{\rm segm} = \int_0^\pi d\beta \sin\beta \int_{-\pi}^{\pi} d\psi \int_{-\pi}^{\pi} d\chi \exp\left\{\frac{1}{a}\left[A\cos\beta + C\cos\psi - \varepsilon(1-\cos\beta)\cos\chi - 2G\sin\frac{\chi}{2}\sin\frac{\psi}{2}\sin\beta\right]\right\}. \quad \text{(S28)}$$

We require that the quadratic form (S1) be positive [2], so that the minimum of the energy corresponds to a straight ($\beta = 0$) and untwisted ($\psi = 0$) conformation. The minimum does not depend on the value of χ. In the limit $a \to 0$ we can expand the trigonometric functions in Eq. (S28) around $\beta = \psi = 0$ and extend the integration domains of these two variables to ∞

$$\begin{aligned} Z_{\rm segm} &\approx e^{(A+C)/a}\int_{-\pi}^{\pi} d\chi \int_0^\infty d\beta\beta \exp\left[-\frac{\beta^2}{2a}(A+\varepsilon\cos\chi)\right]\int_{-\infty}^{\infty} d\psi \exp\left[-\frac{C}{2a}\left(\psi^2 + \frac{2G}{C}\sin\frac{\chi}{2}\beta\psi\right)\right] \\ &= \ldots \frac{e^{(A+C)/a}}{\sqrt{C}}\int_{-\pi}^{\pi} d\chi \int_0^\infty d\beta^2 \exp\left[-\frac{\beta^2}{2a}\left(A+\varepsilon\cos\chi - \frac{G^2}{C}\sin^2\frac{\chi}{2}\right)\right] \\ &= \ldots \frac{e^{(A+C)/a}}{\sqrt{C}}\int_{-\pi}^{\pi} d\chi \frac{d\chi}{A - G^2/2C + (\varepsilon + G^2/2C)\cos\chi} = \ldots \frac{e^{(A+C)/a}}{\sqrt{C}}\left[\left(A - \frac{G^2}{2C}\right)^2 - \left(\varepsilon + \frac{G^2}{2C}\right)^2\right]^{-1/2} \\ &= \ldots \frac{e^{(A+C)/a}}{\sqrt{C}}\left[(A+\varepsilon)\left(A - \varepsilon - \frac{G^2}{C}\right)\right]^{-1/2}, \end{aligned} \quad \text{(S29)}$$

where the dots (...) denote numerical prefactors which can be ignored, since they do not contribute to thermal averages [3].

We are interested in the following averages

$$\langle\cos\beta\rangle = a\frac{\partial}{\partial A}\ln Z_{\rm segm} = 1 - \frac{a}{A}\frac{1 - \dfrac{G^2}{2AC}}{1 - \dfrac{\varepsilon^2}{A^2} - \dfrac{G^2}{AC}\left(1 + \dfrac{\varepsilon}{A}\right)} \equiv 1 - \frac{a}{\kappa_{\rm b}} \quad \text{(S30)}$$

and

$$\langle\cos(\alpha + \gamma - 2\phi_0)\rangle = a\frac{\partial}{\partial C}\ln Z_{\rm segm} = 1 - \frac{a}{2C}\frac{1 - \dfrac{\varepsilon}{A}}{1 - \dfrac{\varepsilon}{A} - \dfrac{G^2}{AC}} \equiv 1 - \frac{a}{2\kappa_{\rm t}}. \quad \text{(S31)}$$

The difference of a factor 2 in the definitions above stems from the differences in the integrations over the Euler angles, with integration elements $d\beta\sin\beta$ and $d\psi$ for bending and twist, respectively. We have defined

$$\boxed{\kappa_{\rm b} = A\frac{1 - \dfrac{\varepsilon^2}{A^2} - \dfrac{G^2}{AC}\left(1 + \dfrac{\varepsilon}{A}\right)}{1 - \dfrac{G^2}{2AC}}} \quad \text{(S32)}$$

and

$$\boxed{\kappa_{\rm t} = C\frac{1 - \dfrac{\varepsilon}{A} - \dfrac{G^2}{AC}}{1 - \dfrac{\varepsilon}{A}},} \quad \text{(S33)}$$

which are Eqs. (3) and (4) of the main paper. These equations show that the bending and twist fluctuations between neighboring segments are governed by *renormalized* bending and torsional stiffnesses $\kappa_{\rm b}$ and $\kappa_{\rm t}$. In the TWLC limit $G, \varepsilon \to 0$ we get $\kappa_{\rm b} = A$ and $\kappa_{\rm t} = C$, while a finite twist-bend coupling ($G \neq 0$) gives $\kappa_{\rm b} < A$ and $\kappa_{\rm t} < C$. This renormalization is induced by thermal fluctuations, resulting in twisting a thermally fluctuating chain ($\kappa_{\rm t} < C$) costing less energy than twisting a straight segment ($\kappa_{\rm t} = C$). Note also that a bending anisotropy in absence of twist-bend

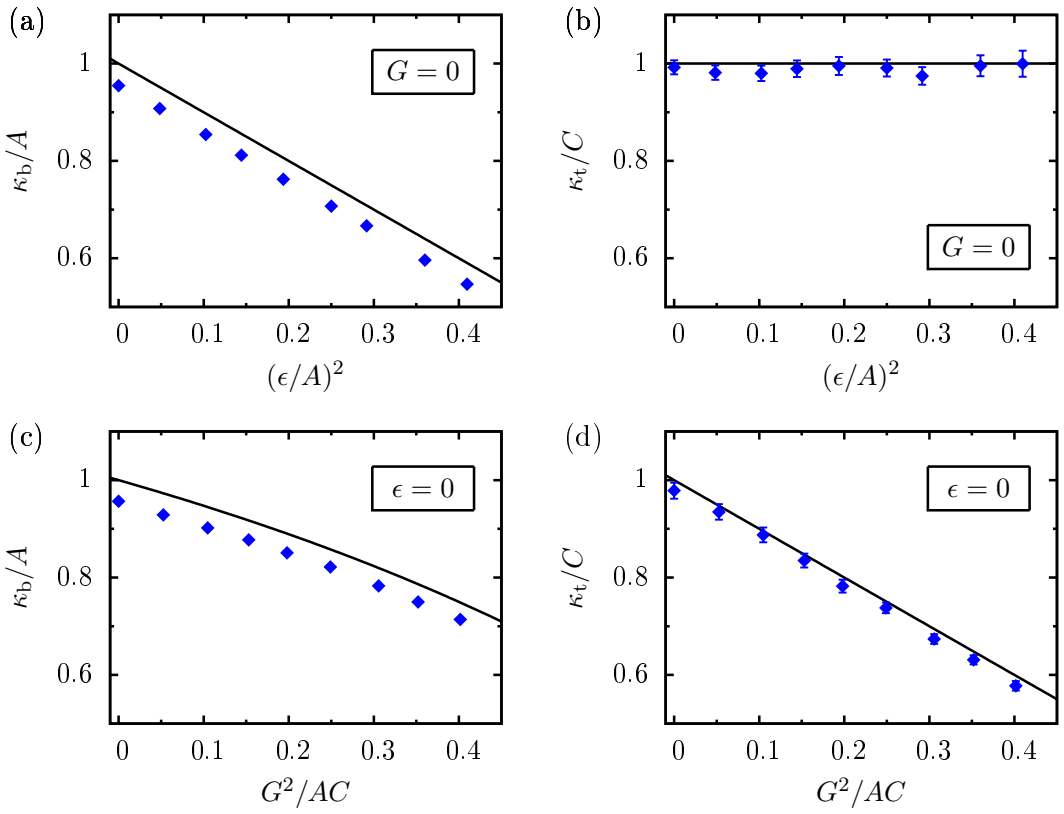

FIG. S1. Comparison between Eqs. (S32) and (S33) (black, solid lines) and computer simulations (blue diamonds), showing the dependence of κ_b and κ_t on the anisotropic bending (a,b) and twist-bend coupling (c,d). In both cases theory and simulations are in good agreement. The error bars are the SEM, and are not shown where they are smaller than the point size.

coupling ($G = 0$ and $\varepsilon \neq 0$) has no effect on the torsional stiffness ($\kappa_t = C$), but it modifies bending as

$$\frac{1}{\kappa_b} = \frac{A}{A^2 - \varepsilon^2} = \frac{1}{2}\left(\frac{1}{A_1} + \frac{1}{A_2}\right), \tag{S34}$$

i.e. the renormalized bending stiffness is the harmonic mean of A_1 and A_2 [4, 5].

Eqs. (S32) and (S33) are exact in the continuum limit $a \to 0$. Here we compare them with simulations in order to test the computer model employed for the numerical calculations. As a first test, we studied the effect of bending anisotropy and twist-bend coupling separately. More specifically, we ran simulations for $G = 0$ and measured the dependence of κ_b and κ_t on ε. The results are summarized in Figs. S1(a) and S1(b), where we also compare with the expressions

$$\frac{\kappa_b}{A} = 1 - \frac{\varepsilon^2}{A^2} \qquad \text{and} \qquad \frac{\kappa_t}{C} = 1, \tag{S35}$$

as predicted by Eqs. (S32) and (S33). We also tested the dependence on G, by setting $\varepsilon = 0$ and comparing with the predictions of Eqs. (S32) and (S33)

$$\frac{\kappa_b}{A} = \frac{1 - \dfrac{G^2}{AC}}{1 - \dfrac{G^2}{2AC}} \qquad \text{and} \qquad \frac{\kappa_t}{C} = 1 - \frac{G^2}{AC}. \tag{S36}$$

The results are shown in Figs. S1(c) and S1(d). In all cases we observe a good agreement between the two, though the computer model seems to slightly underestimate κ_b in a systematic way, compared to Eq. (S33). A possible

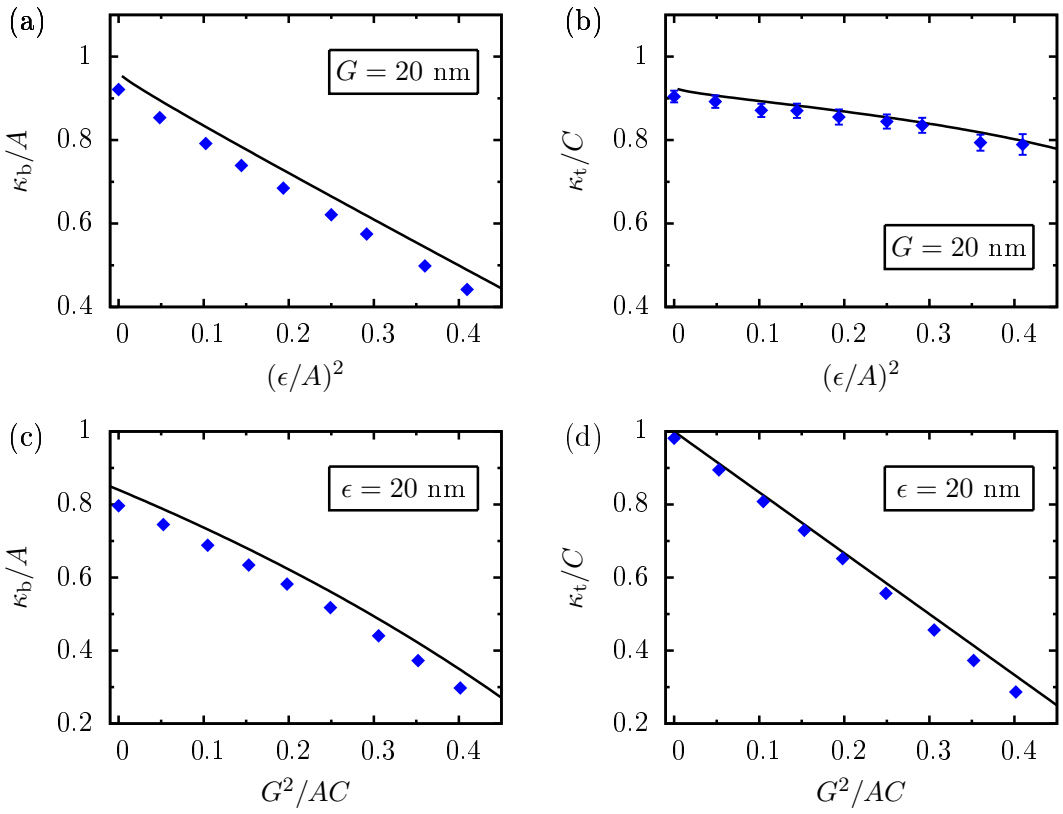

FIG. S2. Comparison between Eqs. (S32) and (S33) (black, solid lines) and computer simulations (blue diamonds), showing how the κ_b and κ_t are affected when one introduces both the anisotropic bending and the twist-bend coupling simultaneously. In (a) and (b) we display the dependence of κ_b and κ_t respectively, on the bending anisotropy ε, with the twist-bend coupling constant being fixed at $G = 20$ nm. In a similar manner, in (c) and (d) we fix the bending anisotropy constant $\varepsilon = 20$ nm and vary G. In all cases, the agreement between theory and simulations is very good. The error bars are the SEM and is not shown where it is smaller than the point size.

origin is the continuum-limit approximation that we introduced in the analytical calculation, as our computer model is discrete.

Furthermore, we tested the combined effect of bending anisotropy and twist-bend coupling, by keeping one of the two properties fixed, while varying the magnitude of the other. More specifically, in Figs. S2(a) and S2(b) we show how κ_b and κ_t depend on ε, when setting $G = 20$ nm. Similarly, in Figs. S2(c) and S2(d) we have taken $\varepsilon = 20$ nm and plotted the G-dependence of the persistence lengths. Again, the agreement between theory and simulations is very good, even under this extreme "softening" of the rod. Thus, we conclude that our computer simulations are in very good agreement with Eqs. (S32) and (S33), apart from a slight systematic deviation in κ_b.

From Eqs. (S30), (S31) one easily obtains the correlation functions. For instance, bending correlations are given by

$$\langle \widehat{\mathbf{e}}_3(0) \cdot \widehat{\mathbf{e}}_3(na) \rangle = \langle \cos\beta_1 \cos\beta_2 \ldots \cos\beta_n \rangle = \langle \cos\beta \rangle^n \equiv e^{-na/l_b}, \tag{S37}$$

where l_b is the bending persistence length. We then have

$$l_b \equiv -\frac{a}{\ln\langle\cos\beta\rangle} = -\frac{a}{\ln\left(1 - \frac{a}{\kappa_b}\right)} \approx \kappa_b, \tag{S38}$$

in the limit $a \to 0$. In a similar manner (see for example [6]) one can define a correlation length associated with twist as

$$l_t \approx 2\kappa_t \tag{S39}$$

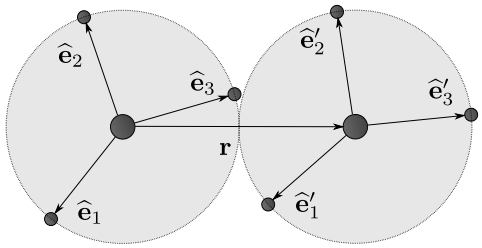

FIG. S3. An schematic example of the DNA computer model used in this work. The molecule is simulated as a series of connected beads, two of which are shown. The beads are separated by a distance $|\mathbf{r}|$, and carry a local orthonormal frame $\{\widehat{\mathbf{e}}_1, \widehat{\mathbf{e}}_2, \widehat{\mathbf{e}}_3\}$, which is represented by three small particles.

COARSE-GRAINED COMPUTER SIMULATIONS OF DNA

Computer simulations of the TWLC and MS model were performed using a coarse-grained bead-and-spring model, similar to the one discussed in Ref. [6], with the addition of twist-bend coupling and anisotropic bending interactions. Each bead is a rigid spherical body, consisting of a core particle and three patches at fixed distance from the core defining a local frame $\{\widehat{\mathbf{e}}_1, \widehat{\mathbf{e}}_2, \widehat{\mathbf{e}}_3\}$. Fig. S3 shows an example of two adjacent beads, together with the two respective frames, denoted by $\{\widehat{\mathbf{e}}_1, \widehat{\mathbf{e}}_2, \widehat{\mathbf{e}}_3\}$ and $\{\widehat{\mathbf{e}}'_1, \widehat{\mathbf{e}}'_2, \widehat{\mathbf{e}}'_3\}$. These beads are connected via a strong finitely extensible nonlinear elastic (FENE) interaction, which keeps their separation distance r very close to a fixed value $|\mathbf{r}| \approx a$. A very strong interaction term is also used in order to align $\widehat{\mathbf{e}}_3$ with $\mathbf{r}$ [6], ensuring that $\widehat{\mathbf{e}}_3$ is the local tangent to the polymer chain. The Ω_i terms are computed from a discretization process, as shown in the previous section. For instance, the calculation of Ω_1^2 (Eq. (S13)) yields

$$\Omega_1^2 = \frac{1 + \widehat{\mathbf{e}}'_1 \cdot \widehat{\mathbf{e}}_1 - \widehat{\mathbf{e}}'_2 \cdot \widehat{\mathbf{e}}_2 - \widehat{\mathbf{e}}'_3 \cdot \widehat{\mathbf{e}}_3}{a^2}. \tag{S40}$$

All other terms in the energy functional (S1) are calculated in a similar way, and can be expressed as scalar products between $\{\widehat{\mathbf{e}}_1, \widehat{\mathbf{e}}_2, \widehat{\mathbf{e}}_3\}$ and $\{\widehat{\mathbf{e}}'_1, \widehat{\mathbf{e}}'_2, \widehat{\mathbf{e}}'_3\}$. In our discretization setup we choose beads with diameter $a = 2.3$ nm corresponding to 6.7 base pairs, which is a good compromise between numerical accuracy and computational efficiency. There is no intrinsic twist, i.e. $\omega_0 = 0$, in the simulations. The two ends of the polymer were attached to an impenetrable surface and a large bead, similarly to a typical MT experiment. We included the effect of the solvent implicitly, by means of Langevin forces [7]. A repulsive Lennard-Jones potential with an effective, hard-core diameter of 3.5 nm [8] was used, in order to avoid distant parts of the polymer from overlapping. The effective torsional stiffness was calculated from the relation $C_{\text{eff}} = L/\sigma_\theta^2$, where L is the contour length of the polymer ($L = 1$ kbp in the simulations) and σ_θ^2 is the variance of the twist angle. All simulations were performed with the Large-scale Atomic/Molecular Massively Parallel Simulator (LAMMPS) [9].

FORCE-EXTENSION SIMULATIONS

In order to test the used parametrization of the MS model, we performed simulations of a dsDNA under an applied, stretching force in the range $f = 0.08 - 6.25$ pN and measured its extension in absence of twist (Fig. S4). We compare between the TWLC with $A = 43$ nm and $C = 110$ nm, and the MS model with the values of parameters used throughout this work, i.e. $A = 56$ nm, $\varepsilon = 10$ nm, $C = 110$ nm and $G = 40$ nm. The MS model with this parametrization fits the C_{eff} data, as shown in the main text, and yields a persistence length of $l_b = 43$ nm, Eq. (S32). Fig. S4 also plots the asymptotic expression of the WLC force-extension curve [10]

$$\frac{f l_b}{k_B T} = \frac{1}{4}\left(1 - \frac{z}{L}\right)^{-2} \tag{S41}$$

and the approximated interpolation formula

$$\frac{f l_b}{k_B T} = \frac{1}{4}\left(1 - \frac{z}{L}\right)^{-2} - \frac{1}{4} + \frac{z}{L}. \tag{S42}$$

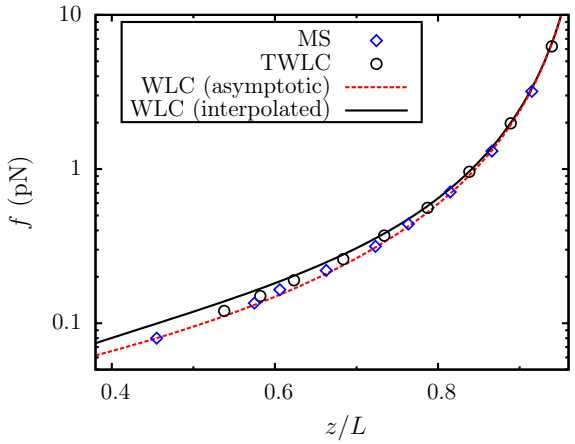

FIG. S4. Force-extension computer simulations of the TWLC ($A = 43$ nm and $C = 110$ nm) and the MS models ($A = 56$ nm, $\varepsilon = 10$ nm, $C = 110$ nm and $G = 40$ nm), together with the interpolated result of Eq. (S42) and its high-force limit of Eq. (S41). Both models are in good agreement with these expessions. The error bars (SEM) are smaller than the size of the points and, thus, not shown.

The latter is known to reproduce within few percents the force-extension experimental data in a wide range of forces and is in good agreement with both the TWLC and the MS models. The conclusion is that the MS model, with the parametrization used throughout this work, is consistent with the measured force-extension curves.

DEPENDENCE OF C_{eff} ON G AND ε

We tested the dependence on G and ε of the effective torsional stiffness as obtained from simulations of the MS model. Figure S5 shows the results of the simulations for (a) fixed G and varying ε and for (b) fixed ε and varying G. C_{eff} depends weakly on ε, while is much more sensitive to a change of G. Figure S5(b) shows that the range $30 \leq G \leq 50$ nm fit the experimental data including error bars, hence our estimate of twist-bend coupling constant is $G = 40 \pm 10$ nm.

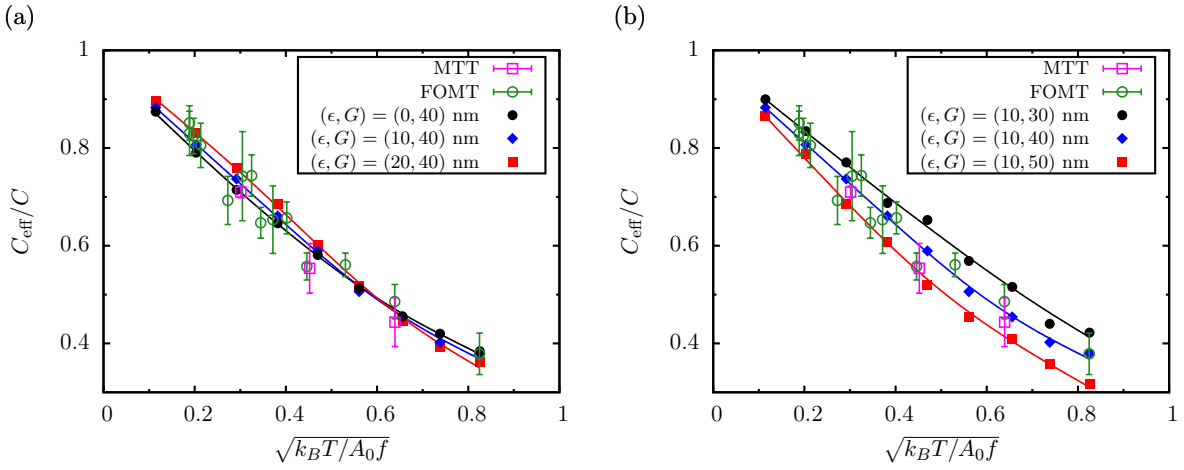

FIG. S5. Effective torsional stiffness C_{eff} obtained from simulations of the MS model as a function of the rescaled variable $\sqrt{k_B T/A_0 f}$ for different values of G and ε. (a) The twist-bend coupling constant is fixed to $G = 40$ nm, and we vary $\varepsilon = 0$, 10 and 20 nm (reduced $\chi^2 = 0.83$, 0.82 and 1.3, respectively). (b) The bending anisotropy is fixed to $\varepsilon = 10$ nm and we vary $G = 30$, 40 and 50 nm (reduced $\chi^2 = 2.1$, 0.82 and 2.5, respectively). The intrinsic torsional stiffness is set to $C = 110$ nm, while A is fixed by imposing $l_b = 43$ nm.

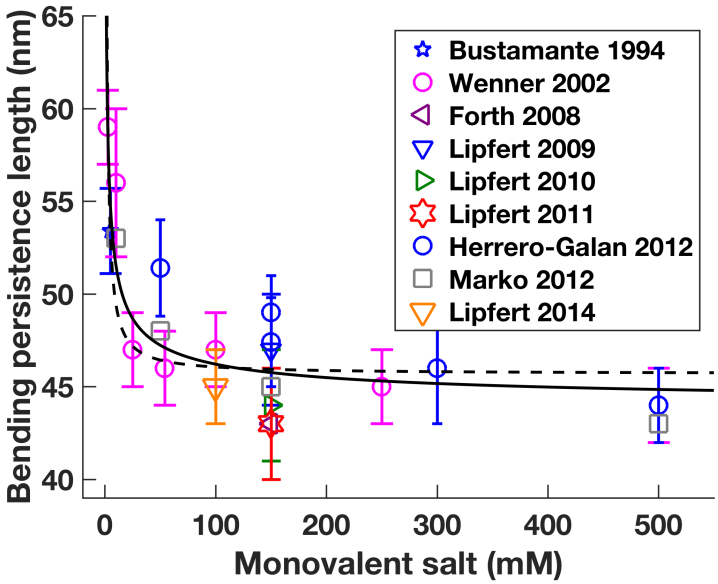

FIG. S6. Dependence of the bending persistence length of dsDNA on the monovalent salt concentration. The plotted data are from Bustamante et al. [11], Wenner et al. [12], Forth et al. [13], Lipfert et al. [14–17], Herrero-Galan et al. [18] and Marko et al. [19]. The salt dependence can be fitted with a function of the form $\kappa_b = \kappa_0 + m[\text{salt}]^{-\alpha}$, where [salt] is the monovalent salt concentration, α is a scaling parameter and κ_0 and m are fitting parameters. According to the models by Odijk [20] and Skolnick and Fixman [21] it is $\alpha = 1$ (fit shown as dashed line), while the model by Barrat and Joanny [22] predicts $\alpha = 1/2$ (fit shown as solid line). The experiments discussed in the main text are at 100 mM and 150 mM monovalent salt, which correspond to a bending persistence length within the range $43 - 48$ nm.

DEPENDENCE OF C_{eff} ON THE BENDING PERSISTENCE LENGTH

The experiments reported in Fig. 2 of the main text are from two independent single-molecule approaches: freely orbiting magnetic tweezers (FOMT) from Ref. [16] and magnetic torque tweezers (MTT) from this work. The DNA construct was the same in both cases (7.9 kbp, as described in Ref. [15]), but the buffer conditions were slightly different, corresponding to 150 mM (FOMT) and 100 mM (MTT) monovalent salt concentration (the details of the MTT experiments are discussed below). As shown in Fig. S6, the bending persistence length at $100 - 150$ mM salt lies typically within the range $43 - 48$ nm. For the data shown in the main text the bending persistence length was chosen to be $\kappa_b = 43$ nm (taken from Ref. [16], obtained from force-extension measurements).

In Fig. S7 we plot with solid lines the results of simulations of the MS model, in which the persistence length was fixed at $\kappa_b = 43$ nm (as in the main text), $\kappa_b = 45$ nm and $\kappa_b = 48$ nm, while keeping $\varepsilon = 10$ nm and $C = 110$ nm. Solid lines are the best fit of the MS model to the experimental data for the given κ_b. All three sets fit equally well the experiments and, as κ_b increases, also the fitted value of G increases (we find $G = 43$ nm and $G = 47$ nm for $\kappa_b = 45$ nm and $\kappa_b = 48$ nm, respectively). Note that an increase in the persistence length leads to a stronger deviation of the Moroz-Nelson theory, plotted with dashed lines in Fig. S7, from the experimental data. Therefore, in order to fit experiments, one needs a higher correction from twist-bend coupling (higher G) for higher κ_b. In conclusion, for the range of values of κ_b corresponding to the experimental conditions, the TWLC does not fit the MT data and one needs a relatively large value of the twist-bend coupling coefficient G to reconcile theory and experiments.

MAGNETIC TORQUE TWEEZERS MEASUREMENTS

Measurements were performed employing a home-built MT setup and a 7.9-kbp DNA construct, as described previously [15]. Specific and torsionally constrained coupling of the dsDNA to magnetic beads (1.0 μm diameter, streptavidin-coated MyOne beads; Life Technologies, USA) and the flow cell surface was achieved through ligation of ~ 600 bp PCR-generated DNA fragments, comprising multiple biotin- and digoxigenin- modified dUTP moieties (Jena Bioscience, Germany), respectively, to the central, unmodified DNA. The labeled dsDNA molecules were attached to

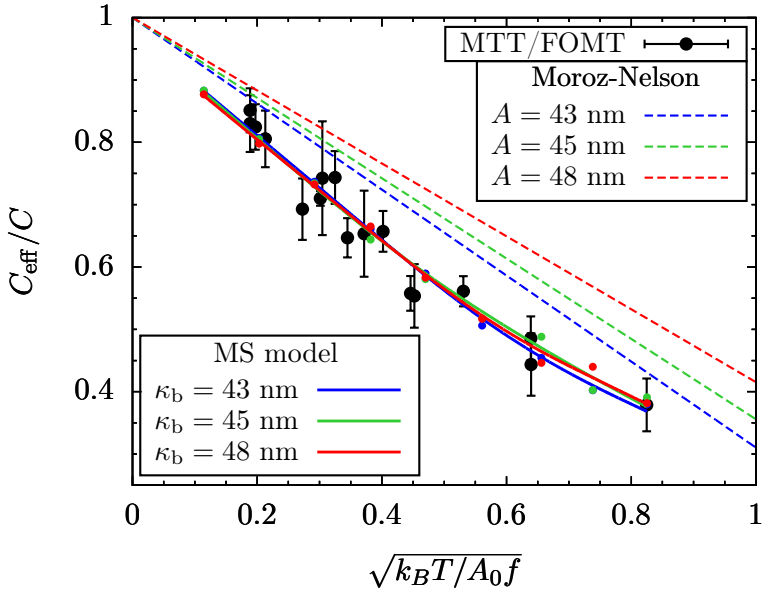

FIG. S7. Solid lines: simulations of $C_{\rm eff}$ for the MS model using different input values of the bending persistence length $\kappa_{\rm b}$. The values we tested (43, 45 and 48 nm with blue, green and red solid interpolated lines, respectively) are representative of the experimental conditions (100 − 150 mM monovalent salt, see Fig. S6) and all yield an excellent fit to the MT data (reduced $\chi^2 = 0.74$, 0.66 and 0.71, respectively). Note that an increase in the persistence length leads to stronger deviations between the TWLC prediction (Moroz-Nelson theory, Eq. (5) of main text, plotted with dashed lines) and the experimental data (reduced $\chi^2 = 6.1$, 9.0 and 12.6 for $\kappa_{\rm b} = 43$, 45 and 48 nm, respectively). As a consequence, the best-fit value of G also increases with $\kappa_{\rm b}$ ($G = 40$, 43 and 47 nm, respectively). In all simulations we fixed $C = 110$ nm and $\varepsilon = 10$ nm (parametrization used in the main text), and chose A according to Eq. (S32).

the streptavidin coated beads by incubating 5 ng of the DNA construct with 2 µL of MyOne beads in a final volume of 100 µl of phosphate buffered saline (PBS; Sigma-Aldrich, USA) for 12 min.

Flow cells were constructed by assembly of two glass coverslips (24 × 60 mm, Carl Roth, Germany) separated by a single parafilm layer. The bottom coverslip was first modified using (3-Glycidoxypropyl)trimethoxysilane (abcr GmbH, Germany), subsequently reacted for one hour with anti-digoxygenin (100 µg/ml in 1× PBS; Roche, Switzerland) and then passivated using BlockAid™ Blocking Solution (Thermoscientific) for one hour. After flushing of the flow cell with PBS buffer, the DNA-bead solution was introduced and allowed to bind for 12 min. Unbound beads are removed from the flow cell by flushing with 800 µL of PBS buffer. To verify that selected beads are bound to a single, torsionally constraint dsDNA tether, several tests were performed using a pair of cubic permanent magnets ($5 \times 5 \times 5$ mm^3; W-05-N50-G, Supermagnete, Switzerland), oriented in a horizontal configuration above the flow cell. First, the external magnets are moved vertically to exert alternating nominal forces of 5 pN and 0.1 pN in order to approximately determine the contour length of the tether. Next, magnets are rotated counterclockwise by 20 turns at high (5 pN) and low (0.5 pN) applied force to identify beads attached via single and fully torsionally constrained dsDNA molecules, using the known rotation-extension behavior of dsDNA [23]. Finally, the flow cell was flushed with ∼ 500 µL of TE buffer (10 mM Tris-HCl, 1 mM EDTA, pH = 8.0) supplemented with 100 mM NaCl, in which the measurements were performed. The relationship between magnet height and applied stretching force was determined from the in-plane fluctuations by spectral analysis as described previously [17, 24].

We performed single-molecule torque measurements using our implementation of magnetic torque tweezers (MTT), a variant of MT that uses a cylindrical magnet with a small additional side magnet to exert a slightly tilted, vertical magnetic field [15]. This field configuration provides a weak rotational trap for the bead, while applying an upward pulling force. At magnet heights of 3, 4 and 5 mm, corresponding to applied forces of 0.9, 0.4 and 0.2 pN, respectively, we probed the extension and torque response [15, 17] of the DNA molecules upon changing the linking number in steps of two turns, for a total number of 24 turns symmetrically around zero turns, corresponding to the torsionally relaxed molecule. Multiple single-molecule torque and extension measurements were averaged; the data shown correspond to 21, 81, and 32 independent molecules for the 0.2, 0.4 and 0.9 pN data, respectively.

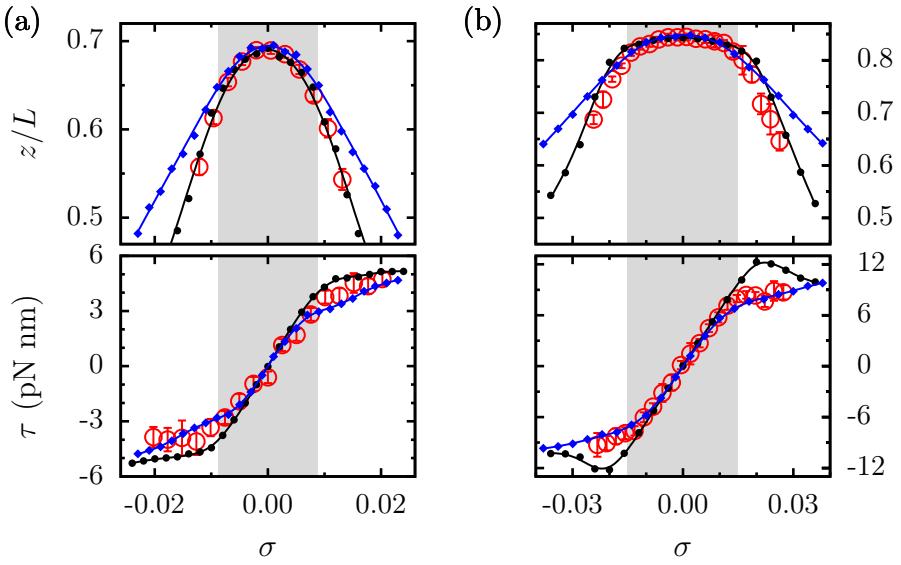

FIG. S8. Relative extension z/L and torque τ, as functions of the supercoiling density σ, for two different forces (a) $f = 0.2$ pN and (b) $f = 0.9$ pN. Open, red circles are from MT experiments, full, black circles from TWLC and full, blue triangles from MS simulations. The shaded areas correspond to the estimated pre-buckling regime. The figures show the same features as Fig. 3 of the main text.

For the overlay, a shift offset was applied to the extension vs. turns traces, such that the extension-rotation curves are centered around zero turns for small forces (< 1 pN). The same shift was applied to the corresponding molecular torque data. Similarly, a constant extension offset was applied to the extension data to correct for slightly different attachment geometries of the DNA to the magnetic beads. As a consequence, the absolute extension has a larger uncertainty than the relative extension measurements, which rely on the look-up table based Z-tracking in the magnetic tweezers with a tracking accuracy of ~ 1 nm [25, 26].

ADDITIONAL EXTENSION AND TORQUE EXPERIMENTS AND SIMULATIONS

Besides the extension and torque data presented in Fig. 3 of the main text, we repeated the experiments and simulations for two different forces. Figure S8 shows the additional plots for the two forces (a) $f = 0.2$ pN and (b) $f = 0.9$ pN. These data show a similar behavior to Fig. 3 of the main text and confirm that the torque is more accurately reproduced by the MS model, whereas the post-buckling extension agrees with the the TWLC simulation data.

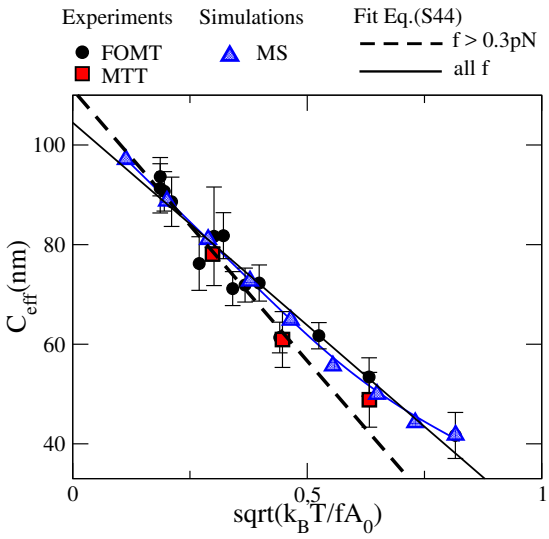

FIG. S9. Determination of the intrinsic torsional stiffness C from linear extrapolation of the experimental $C_{\rm eff}$ vs. force data. Fitting a function of the form $C_{\rm eff} = C + \Gamma/\sqrt{f}$ to the experimental data (same as in Fig. (2) of the main text), allows us to extract C. Extrapolations using all data give $C = 105$ nm (solid line), while if we restrict to forces $f > 0.3$ pN we get $C = 110$ nm (dashed line). Our final estimate is $C = 110 \pm 5$ nm.

EXPERIMENTAL DETERMINATION OF THE INTRINSIC TORSIONAL STIFFNESS C OF DNA

Several experimental techniques, such as magnetic and optical tweezers, cyclization rates and topoisomer distributions have been used in the past in order to determine the value of the intrinsic torsional stiffness C. Table I gives a concise overview, with references, of the measured values from several such studies. As shown in the Table there is a wide variation in the estimates.

The experimental techniques can be divided into two distinct families, depending on whether there is a stretching force applied to DNA or not. One central result of the current study is that the MS model predicts two distinct values of the torsional stiffness: at high stretching forces twist is governed by the intrinsic stiffness which we estimate as $C = 110$ nm, while bending fluctuations in an unstretched DNA renormalize the stiffness to a value $\kappa_{\rm t} = 75$ nm. This conclusion is supported by the experimental data reported in Table I.

If the DNA is elongated by a sufficiently strong force, as in magnetic or optical tweezers, bending fluctuations are suppressed ($\Omega_1 \approx \Omega_2 \approx 0$) and both the TWLC and the MS models converge to the twistable rigid rod limit

$$\beta E_{\rm TWLC} \approx \beta E_{\rm MS} \approx \frac{C}{2}\int_0^L \Omega_3^2\, ds - \beta f L, \tag{S43}$$

where twist stiffness is governed by the parameter C. In practice one can estimate C from the high-force limit of $C_{\rm eff}$. Figure S9 shows an extrapolation based on a two-parameter fit

$$C_{\rm eff}(f) = C + \frac{\Gamma}{\sqrt{f}}, \tag{S44}$$

with C and Γ being the fitting parameters. As shown in the figure, it is convenient to plot $C_{\rm eff}(f)$ vs. $1/\sqrt{f}$ where the fit has the shape of a straight line. The analysis yields $C = 110 \pm 5$ nm, which is the value used throughout the paper.

Extrapolations of C from experimental data sometimes use the Moroz-Nelson curve

$$C_{\rm eff}(f) = C\left(1 - \frac{C}{4A}\sqrt{\frac{k_B T}{fA}}\right), \tag{S45}$$

with C as a free fitting parameter, A being the fixed persistence length. This is the procedure used to obtain C from magnetic and optical tweezers data reported in the first four rows of Table I. In this fit one assumes that the dsDNA

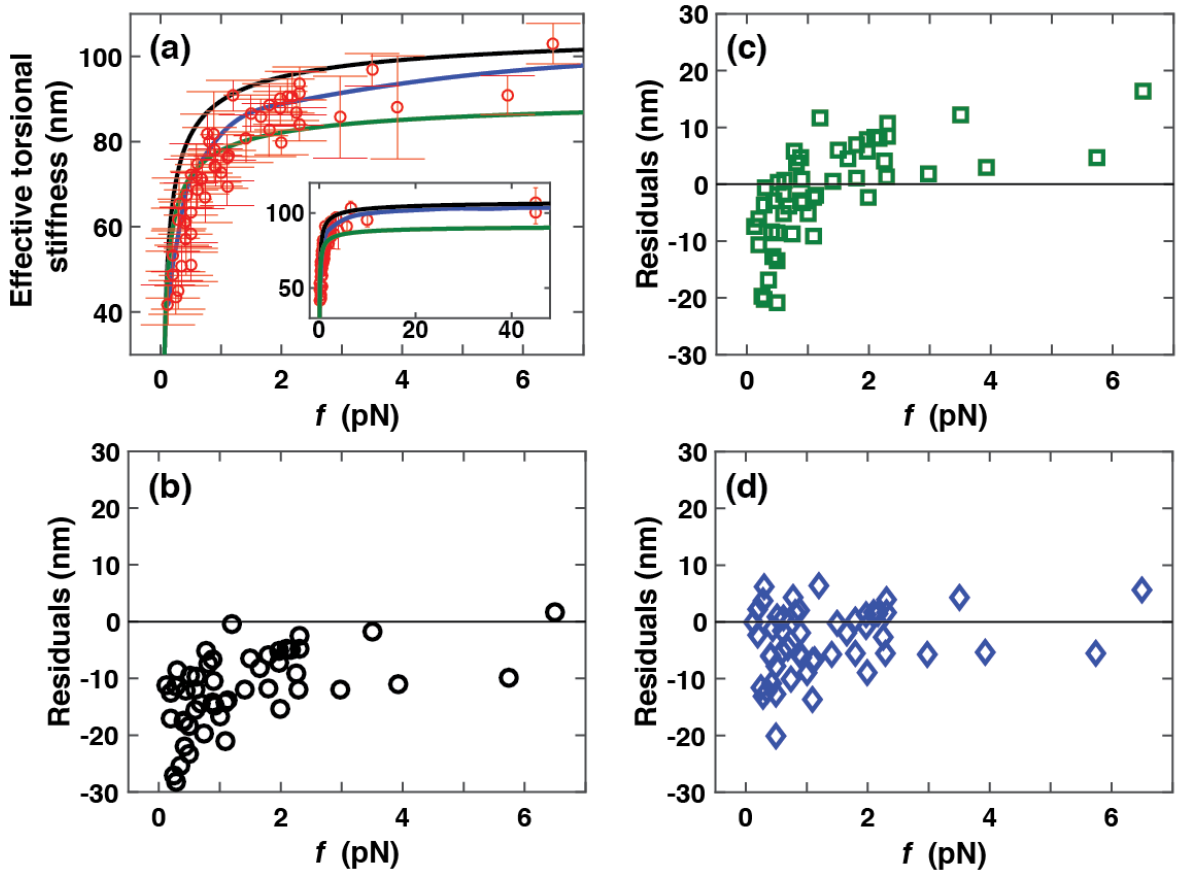

FIG. S10. Comparison of the TWLC (using the Moroz and Nelson formula, Eq. (5) of main text) and the MS model to all available single-molecule torsional stiffness data [13, 15–17, 27–31]. (a) Red symbols are all available single-molecule data on the torsional stiffness of DNA, for which a clear stretching force can be assigned. The black line is the prediction of the Moroz and Nelson formula, taken to third order (see [32]), with $A = 45$ nm and a (limiting value) $C = 110$ nm (reduced $\chi^2 = 14.4$). The green line is a fit of the Moroz and Nelson formula to the data with C treated as a fitting parameter, yielding $C = 92.2$ nm (reduced $\chi^2 = 4.0$). The blue line is the prediction of the MS model with $G = 40$ nm (see main text; reduced $\chi^2 = 2.9$). (b-d) Residuals of the fits in panel a, defined as $C_{\text{eff, experiment}} - C_{\text{eff, theory}}$. (b) Residuals for the Moroz and Nelson formula with fixed A and C. (c) Residuals for the Moroz and Nelson formula with the (high force) value for C fit to the data. It is apparent that the residuals do not scatter symmetrically about zero for neither of the two version of the Moroz and Nelson formula. (d) Residuals for the MS model with $G = 40$ nm. Not only does this model achieve the lowest χ^2, but the residuals also scatter clearly more symmetrically about zero.

is described by the TWLC, while Eq. (S44) is less constraining, assuming only that the asymptotic corrections to $C_{\text{eff}}(f)$ at high forces are of the order $1/\sqrt{f}$.

Fig. S10(a) shows a comparison between all available C_{eff} data and the Moroz-Nelson theory of the TWLC, using the two different fitting procedures (i.e. Eqs. (S44) and (S45)). We compare them to the predictions of the MS model, presented in the main text. Calculating the reduced χ^2 value, in combination with plotting the corresponding residuals (Fig. S5(b-d)), leads us to the conclusion that the TWLC cannot account for the experimental data. It is only when using the MS model, with the high-force extrapolated value of C described above, that we obtain a quantitative fit to the experimental data.

Method	C (nm)	κ_t (nm)
$C_{\rm eff}$ fit Eq.(S45) from OT [13]	100	
$C_{\rm eff}$ fit Eq.(S45) from OT [28]	102	
$C_{\rm eff}$ fit Eq.(S45) from MT [15]	109	
$C_{\rm eff}$ fit Eq.(S45) from MT [30]	97	
Extension-rotation curves [33]	120	
Extension-rotation curves [34]	109	
Extension-rotation curves [35]	85	
Stretching under- and overwound DNA [36]	86	
High-force $C_{\rm eff}$ from RBA [27]	100-105	
High-force $C_{\rm eff}$ from RBA [31]	96	
Force-extension of twisted DNA [37]		75
Cyclization rates [38]		58
Cyclization rates [39]		83
Cyclization rates [40]		49
Topoisomer distribution [41]		71
Supercoils free energies [42]		74
FPA [43]		46
FPA [44]		53
Spin label [45]		36

TABLE I. Torsional stiffness measured with different techniques. Abbreviations used: OT (Optical tweezers), MT (Magnetic tweezers), RBA (Rotor bead assay) and FPA (Fluorescence polarization anisotropy). According to the TWLC model all these techniques are expected to measure the intrinsic torsional stiffness C. According to the MS model, instead, in absence of stretching forces and due to bending fluctuations, the torsional stiffness gets renormalized to a lower value $\kappa_t < C$, given by Eq. (S33). At strong stretching the bending fluctuations are suppressed and the MS model predicts that one should measure C. We estimate $C = 110$ nm and $\kappa_t = 75$ nm. The data in the table are put in two different columns, separating experiments sampling twists under stretching forces (under the column C) and without applied forces (under the column κ_t). Despite some experimental variability, the data support the MS model predictions. Some remarks: Ref. [37] fits force extension curves at fixed supercoil density in a region of small tension ($f < 0.5$ pN, see Fig. 10) therefore we expect that it samples the renormalized torsional stiffness κ_T. FPA and spin label techniques estimate the torsional stiffness from torsional dynamics, and need as input a model of dynamics as well.

[1] J. Marko and E. Siggia, Macromolecules **27**, 981 (1994).

[2] A quadratic form in the variable Ω_i is a homogeneous polynomial of degree two in those variables. It can be written in general by means of a symmetric matrix M_{ij} as $\sum_{ij} \Omega_i M_{ij} \Omega_j$. The quadratic form is said to be positive if the matrix M has positive eigenvalues. We require positivity in order for the system to be stable. In this case $\Omega_i = 0$ corresponds to the minimum value of the form.

[3] There is an approximation which was not explicitly mentioned in the calculation. In the original partition function α and γ vary in the domain $-\pi \leq \alpha \leq \pi$ and $-\pi \leq \gamma \leq \pi$. When changing variables to ψ and χ the integration domain becomes a square with the sides tilted of 45° with respect to the ψ and χ axes. In Eq. (S29) we integrate on $-\infty < \psi < \infty$ and $-\pi \leq \chi \leq \pi$. The extension of the integration of ψ to the whole real domain is justified by the Gaussian approximation.

This is a good approximation except at the two "edges" of the original integration domain $\psi = 0$, $\chi = \pm\pi$. In can be shown that the correct calculation produces higher-order terms in the discretization length a, compared to the result of (S29).

[4] F. Lankaš, J. Šponer, P. Hobza, and J. Langowski, J. Mol. Biol. **299**, 695 (2000).
[5] B. Eslami-Mossallam and M. Ejtehadi, J. Chem. Phys. **128**, 125106 (2008).
[6] C. Brackley, A. Morozov, and D. Marenduzzo, J. Chem. Phys. **140**, 135103 (2014).
[7] R. Zwanzig, *Nonequilibrium Statistical Mechanics* (Oxford University Press, 2001).
[8] V. V. Rybenkov, N. R. Cozzarelli, and A. V. Vologodskii, Proc. Natl. Acad. Sci. USA **90**, 5307 (1993).
[9] S. Plimpton, J. Comput. Phys. **117**, 1 (1995).
[10] J. F. Marko and E. D. Siggia, Macromolecules **28**, 8759 (1995).
[11] C. Bustamante, J. F. Marko, E. D. Siggia, S. Smith, *et al.*, Science **265**, 1599 (1994).
[12] J. R. Wenner, M. C. Williams, I. Rouzina, and V. A. Bloomfield, Biophys. J. **82**, 3160 (2002).
[13] S. Forth, C. Deufel, M. Y. Sheinin, B. Daniels, J. P. Sethna, and M. D. Wang, Phys. Rev. Lett. **100**, 148301 (2008).
[14] J. Lipfert, X. Hao, and N. H. Dekker, Biophys. J. **96**, 5040 (2009).
[15] J. Lipfert, J. W. Kerssemakers, T. Jager, and N. H. Dekker, Nat. Methods **7**, 977 (2010).
[16] J. Lipfert, M. Wiggin, J. W. Kerssemakers, F. Pedaci, and N. H. Dekker, Nat. Commun. **2**, 439 (2011).
[17] J. Lipfert, G. M. Skinner, J. M. Keegstra, T. Hensgens, T. Jager, D. Dulin, M. Köber, Z. Yu, S. P. Donkers, F.-C. Chou, R. Das, and N. H. Dekker, Proc. Natl. Acad. Sci. USA **111**, 15408 (2014).
[18] E. Herrero-Galan, M. E. Fuentes-Perez, C. Carrasco, J. M. Valpuesta, J. L. Carrascosa, F. Moreno-Herrero, and J. R. Arias-Gonzalez, J. Am. Chem. Soc. **135**, 122 (2012).
[19] J. F. Marko, Physica A: Statistical Mechanics and its Applications **418**, 126 (2015).
[20] T. Odijk, J. Polym. Sci. Part B Polym. Phys. **15**, 477 (1977).
[21] J. Skolnick and M. Fixman, Macromolecules **10**, 944 (1977).
[22] J. L. Barrat and J. F. Joanny, EPL **24**, 333 (1993).
[23] T. Strick, J.-F. Allemand, D. Bensimon, A. Bensimon, and V. Croquette, Science **271**, 1835 (1996).
[24] A. J. Te Velthuis, J. W. Kerssemakers, J. Lipfert, and N. H. Dekker, Biophys. J. **99**, 1292 (2010).
[25] C. Gosse and V. Croquette, Biophys. J. **82**, 3314 (2002).
[26] I. Vilfan, J. Lipfert, D. Koster, S. Lemay, and N. Dekker, in *Handbook of Single-Molecule Biophysics* (Springer, 2009) pp. 371–395.
[27] Z. Bryant, M. D. Stone, J. Gore, S. B. Smith, N. R. Cozzarelli, and C. Bustamante, Nature **424**, 338 (2003).
[28] L. Oroszi, P. Galajda, H. Kirei, S. Bottka, and P. Ormos, Phys. Rev. Lett. **97**, 058301 (2006).
[29] F. Mosconi, J. F. Allemand, D. Bensimon, and V. Croquette, Phys. Rev. Lett. **102**, 078301 (2009).
[30] D. J. Kauert, T. Kurth, T. Liedl, and R. Seidel, Nano Lett. **11**, 5558 (2011).
[31] F. C. Oberstrass, L. E. Fernandes, and Z. Bryant, Proc. Natl. Acad. Sci. U.S.A. **109**, 6106 (2012).
[32] J. C. Gore, *Single-molecule studies of DNA twist mechanics and gyrase mechanochemistry*, Ph.D. thesis, University of California (2005).
[33] J. D. Moroz and P. Nelson, Proceedings of the National Academy of Sciences **94**, 14418 (1997).
[34] J. D. Moroz and P. Nelson, Macromolecules **31**, 6333 (1998).
[35] C. Bouchiat and M. Mézard, Phys. Rev. Lett. **80**, 1556 (1998).
[36] T. Strick, D. Bensimon, and V. Croquette, Genetica **106**, 57 (1999).
[37] A. V. Vologodskii and J. F. Marko, Biophys. J. **73**, 123 (1997).
[38] D. Shore and R. L. Baldwin, J. Mol. Biol. **170**, 957 (1983).
[39] S. D. Levene and D. M. Crothers, J. Mol. Biol. **189**, 61 (1986).
[40] W. H. Taylor and P. J. Hagerman, J. Mol. Biol. **212**, 363 (1990).
[41] D. Shore and R. L. Baldwin, J. Mol. Biol **170**, 983 (1983).
[42] A. V. Vologodskii, V. V. Anshelevich, A. V. Lukashin, and M. D. Frank-Kamenetskii, Nature **280**, 294 (1979).
[43] P. R. Selvin, D. N. Cook, *et al.*, Science **255**, 82 (1992).
[44] P. J. Heath, J. B. Clendenning, B. S. Fujimoto, and M. J. Schurr, J. Mol. Biol. **260**, 718 (1996).
[45] I. Hurley, P. Osei-Gyimah, S. Archer, C. Scholes, and L. Lerman, Biochem. **21**, 4999 (1982).